# Supporting Information

## Defect-Induced Dense Amorphous/Crystalline Heterophase Enables High-Rate and Ultra-Stable Sodium Storage

Sahar Osman, Chao Peng*, Fangkun Li, Haoliang Chen, Jiadong Shen, Zeming Zhong, Wenjie Huang, Dongfeng Xue, and Jun Liu*

S. Osman, F. Li, H. Chen, J. Shen, Z. Zhong, W. Huang, Prof. J. Liu

School of Materials Science and Engineering and Guangdong Provincial

Key Laboratory of Advanced Energy Storage Materials

South China University of Technology

Guangzhou, Guangdong 510641, China

Email: msjliu@scut.edu.cn

Dr. C. Peng, Prof. D. Xue

Multiscale Crystal Materials Research Center

Shenzhen Institute of Advanced Technology

Chinese Academy of Science, Shenzhen 518055, China

Email: chao.peng@siat.ac.cn

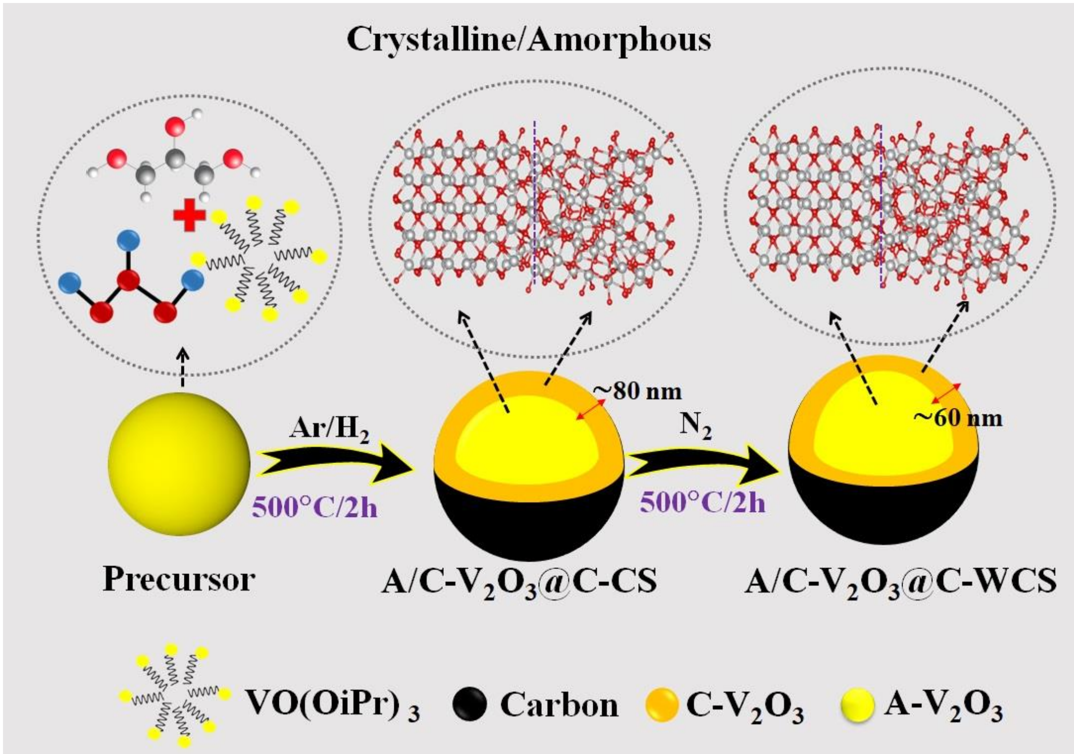


**Figure S1.** Schematic illustration of the synthesis of A/C-$V_2O_3$@C-CS and A/C-$V_2O_3$@C-WCS.

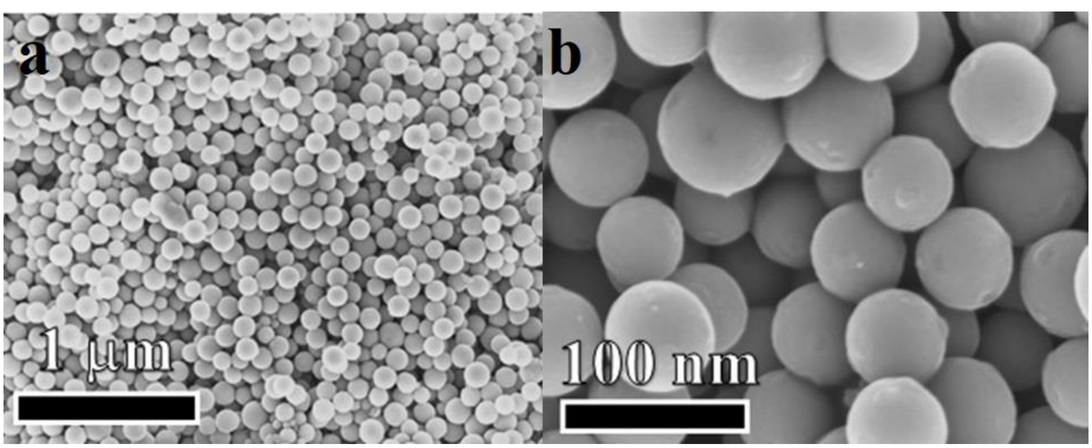


**Figure S2.** (a, b) Low/high magnification SEM images of vanadium-glycerate precursor.

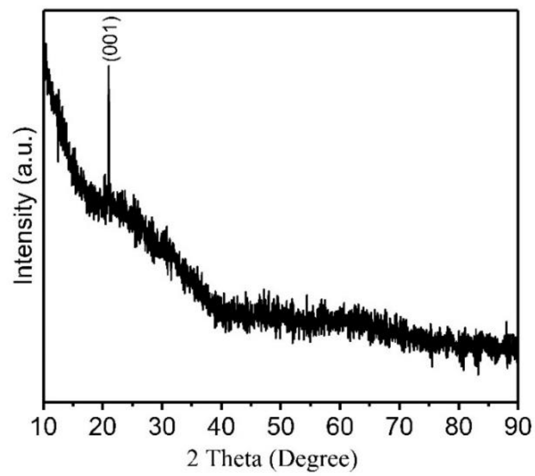


**Figure S3.** XRD pattern of V-glycerate spheres.

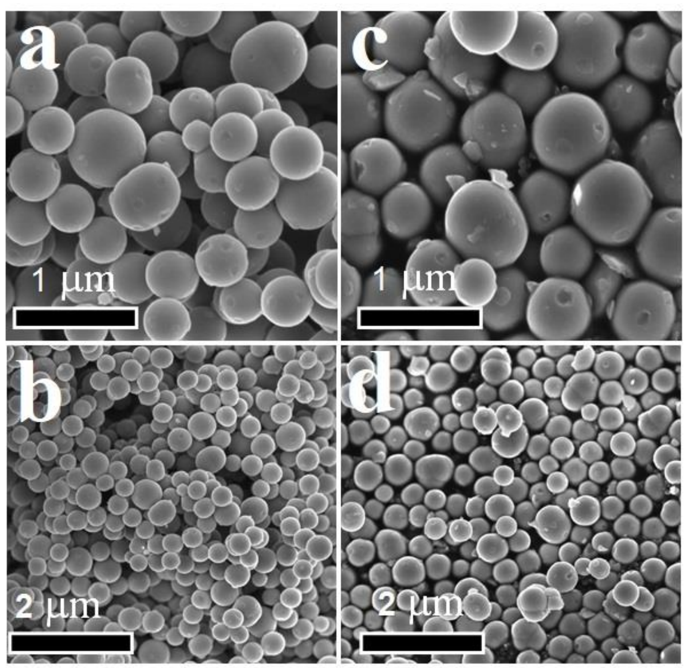


**Figure S4.** High/low-magnification SEM images of (a, b) A/C-$V_2O_3$@C-CS and (c, d) A/C-$V_2O_3$@C-WCS.

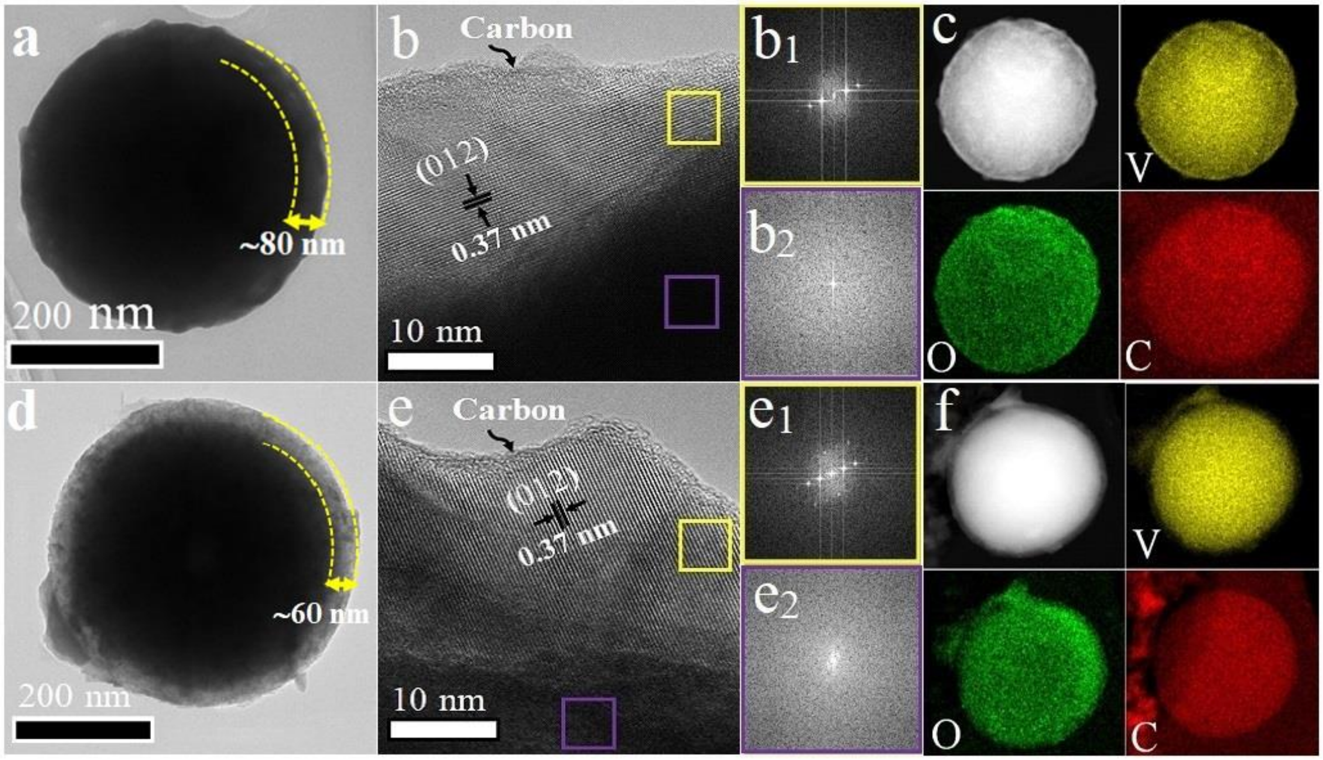


**Figure S5. Morphology and characterizations of A/C-$V_2O_3$@C-CS and /C-$V_2O_3$@C-WCS** (a, d) TEM, (b, e) HRTEM images. ($b_1$, $e_1$) FFT patterns are taken from the corresponding yellow square and ($b_2$, $e_2$) violet square areas in (b, e), and (c, f) EDS mapping images of core-shell A/C-$V_2O_3$@C-CS and A/C-$V_2O_3$@C-WCS, respectively.

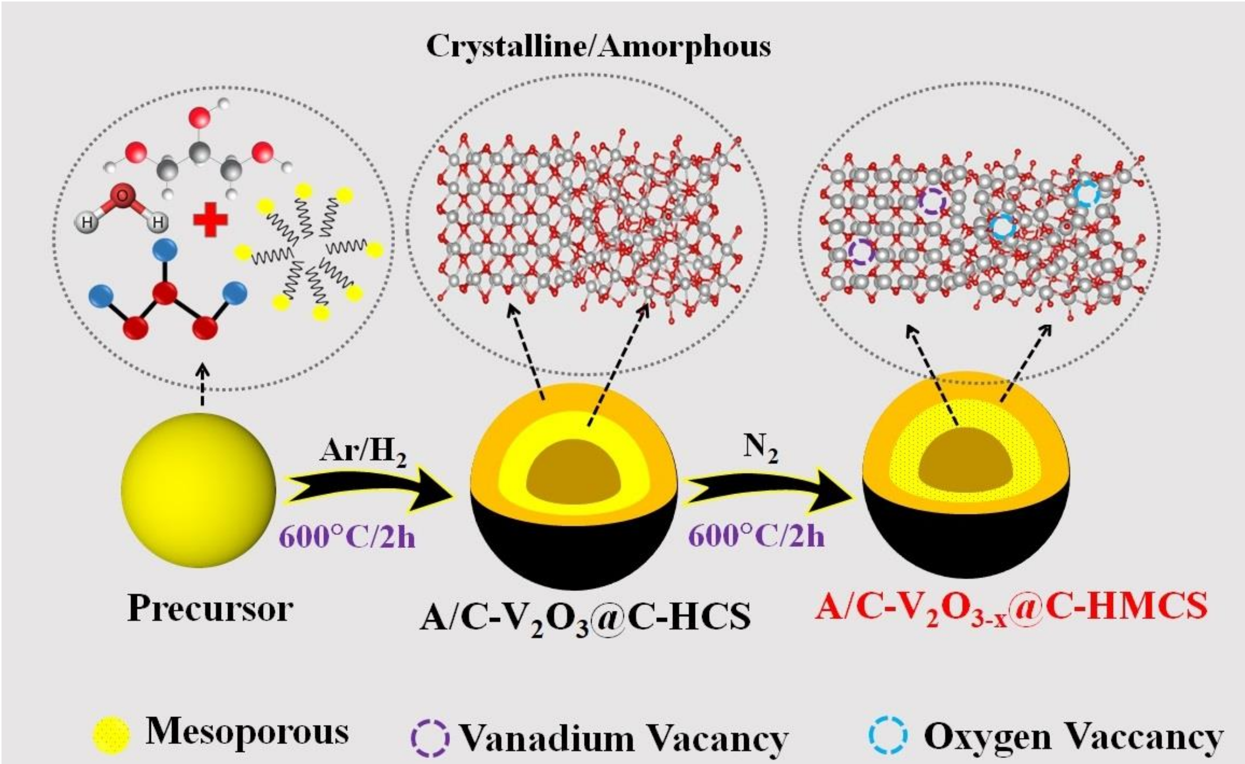


**Figure S6.** Schematic illustration of the synthesis of A/C-$V_2O_3$@C-HCS and A/C-$V_2O_{3-x}$@C-HMCS.

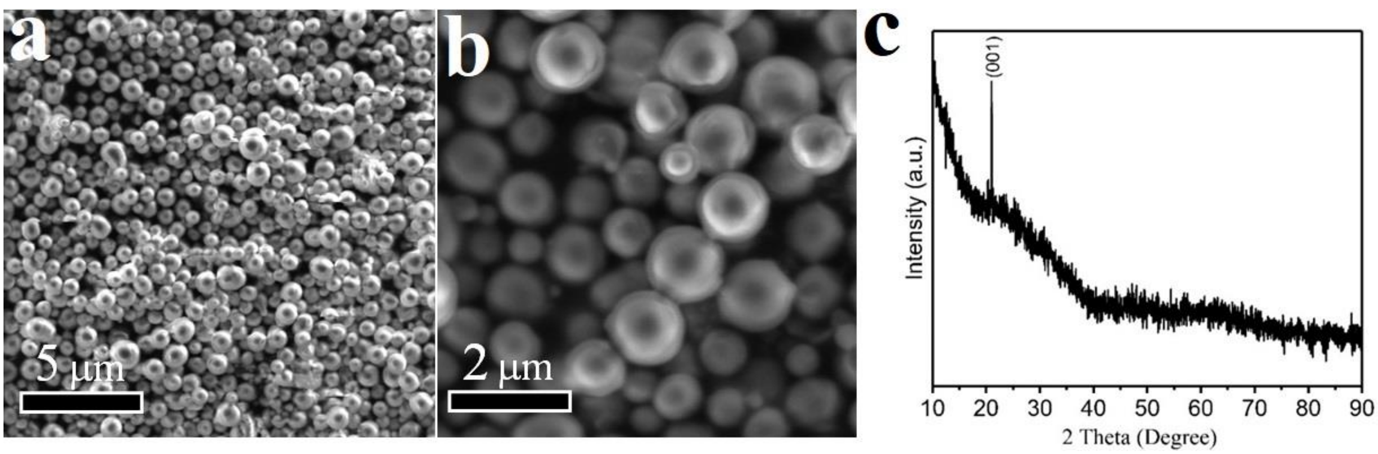


**Figure S7.** (a, b) Low/high magnification SEM images of vanadium hydrate-glycerate precursor. c) its XRD pattern.

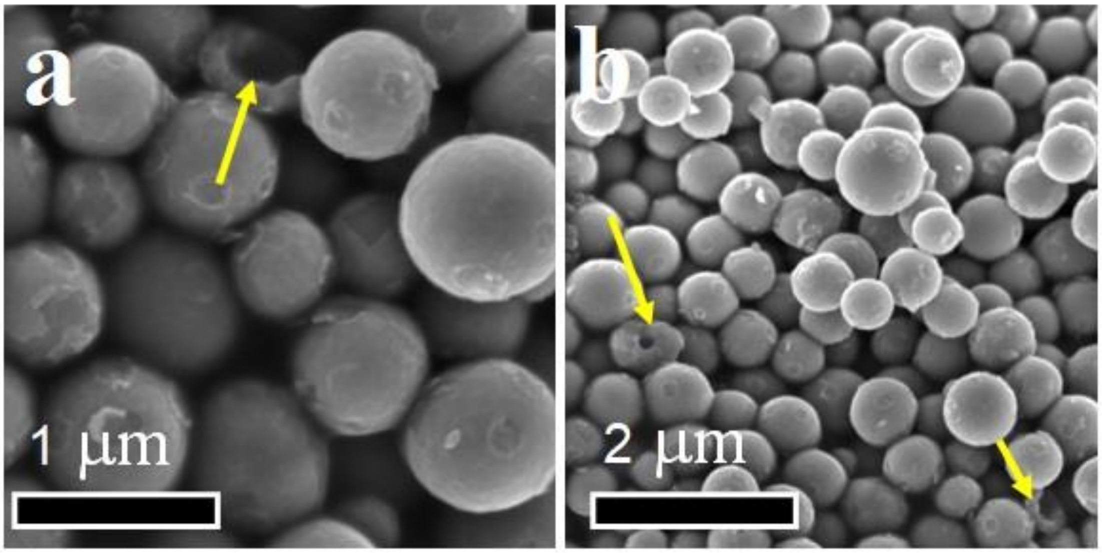


**Figure S8.** (a, b) High/low-magnification SEM images of A/C-$V_2O_3$@C-HCS.

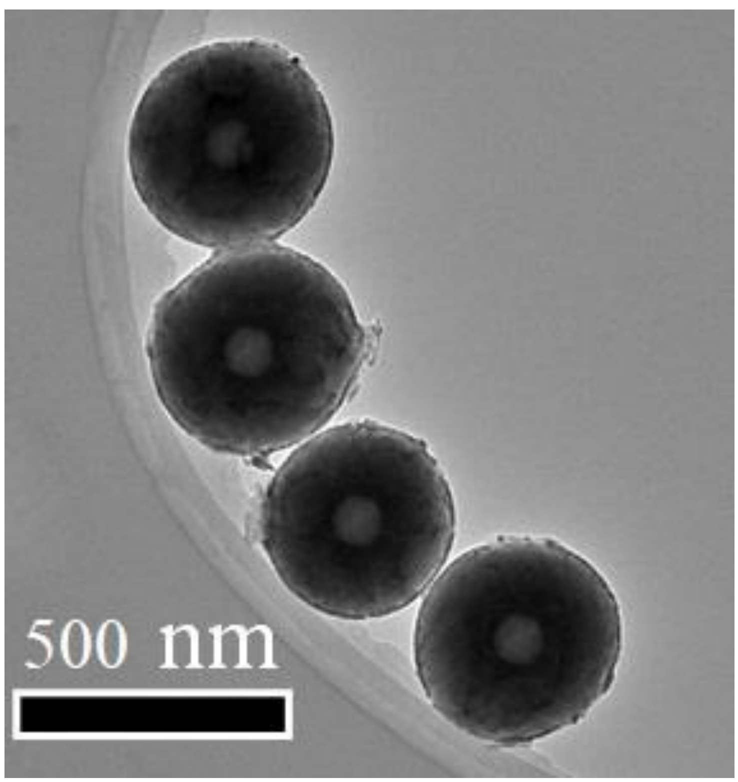


**Figure S9.** TEM image of A/C-$V_2O_3$@C-HCS.

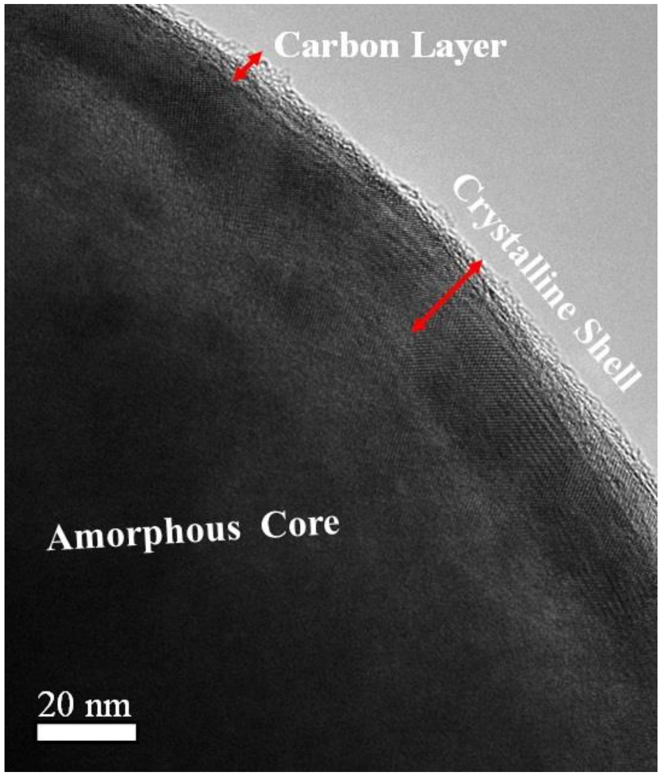


**Figure S10.** HTEM image of A/C-$V_2O_3$@C-HCS.

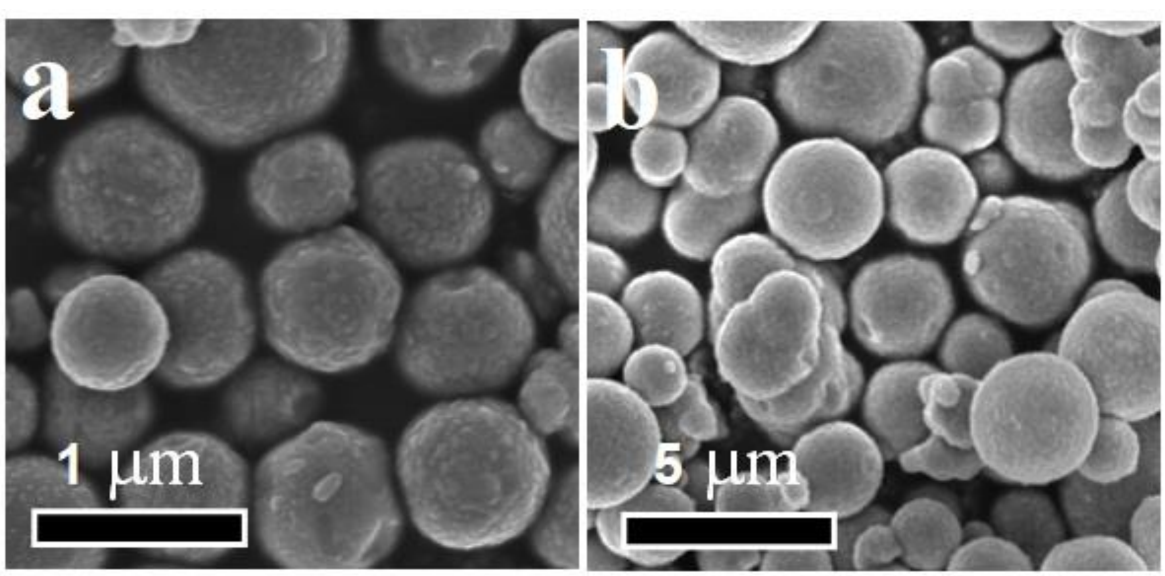


**Figure S11.** (a, b) High/low-magnification SEM images of A/C-$V_2O_{3-x}$@C-HMCS.

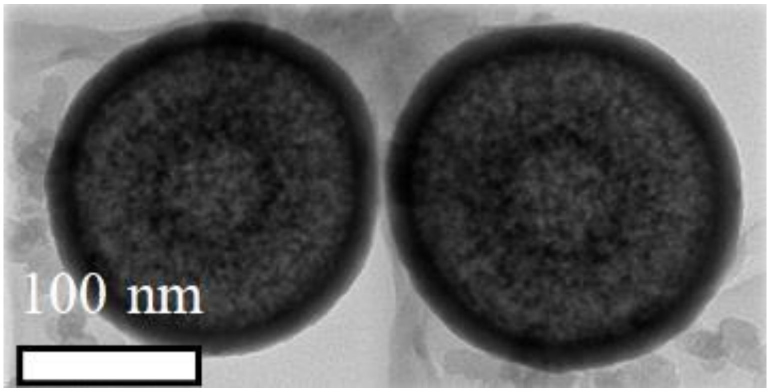


**Figure S12.** TEM image of A/C-$V_2O_{3-x}$@C-HMCS.

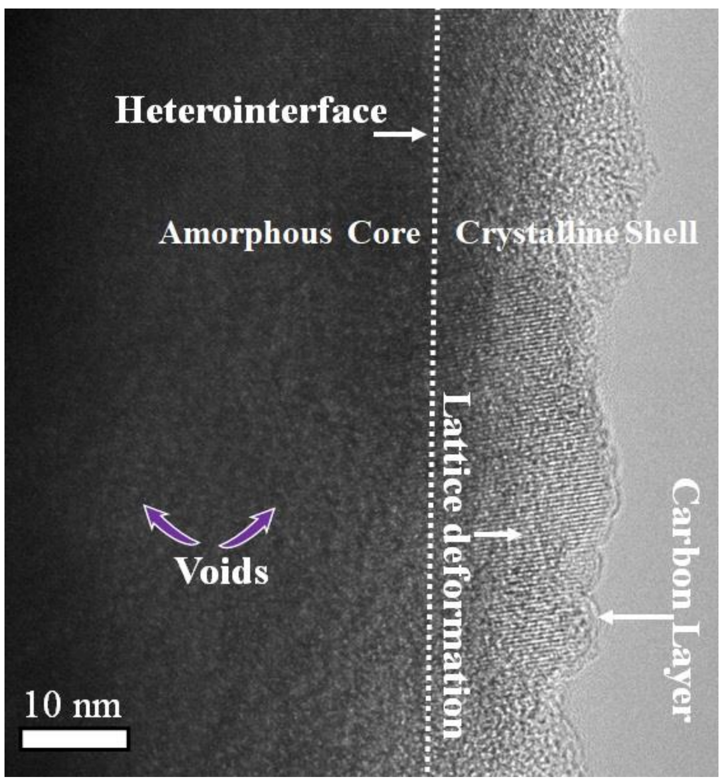


**Figure S13.** HTEM image of A/C-$V_2O_{3-x}$@C-HMCS.

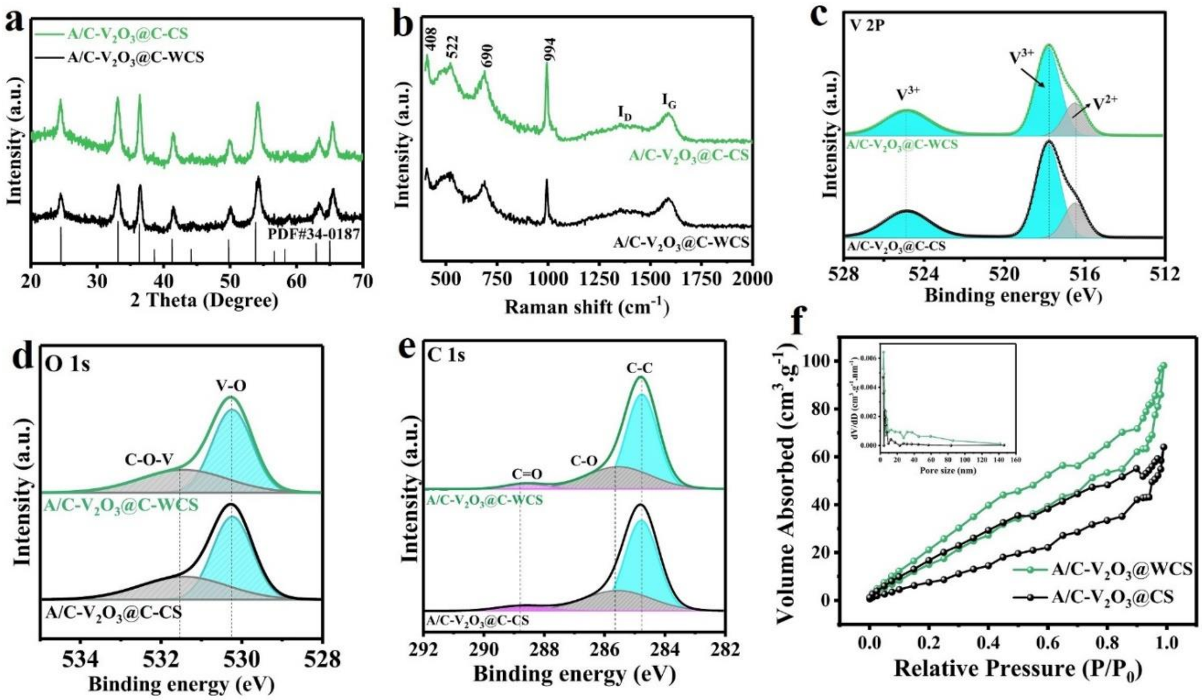


**Figure S14. Structural characterizations of A/C-$V_2O_3$@C-CS and A/C-$V_2O_3$@C-WCS:** (a) XRD patterns, (b) Raman spectra, high-resolution spectra of :(c) V 2p, (d) O 1s, (e) C 1s. (f) $N_2$ adsorption-desorption isotherms and their pore size distributions (inset).

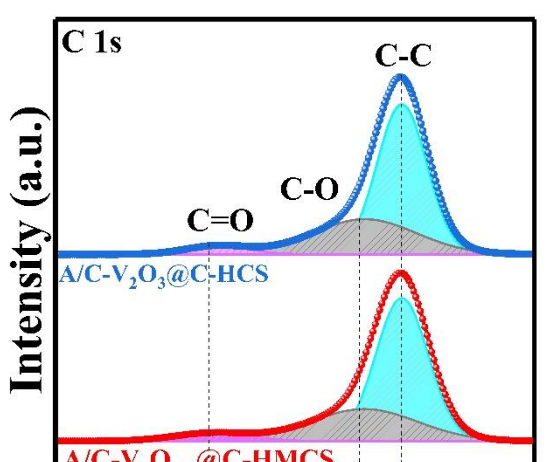


**Figure S15.** C 1s high-resolution spectra of A/C-$V_2O_3$@C-HCS and A/C-$V_2O_{3-x}$@C-HMCS.

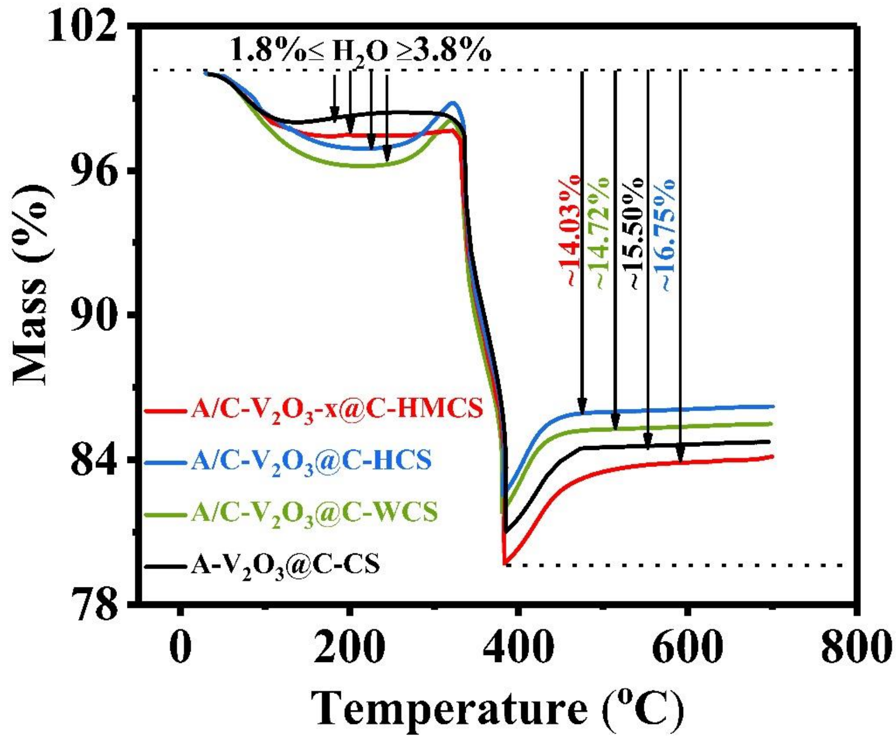


**Figure S16.** Thermogravimetric analysis (TGA) curve for the A/C-$V_2O_3$@C-CS, A/C-$V_2O_3$@C-WCS, A/C-$V_2O_3$@C-HCS, and A/C-$V_2O_{3-x}$@C-HMCS.

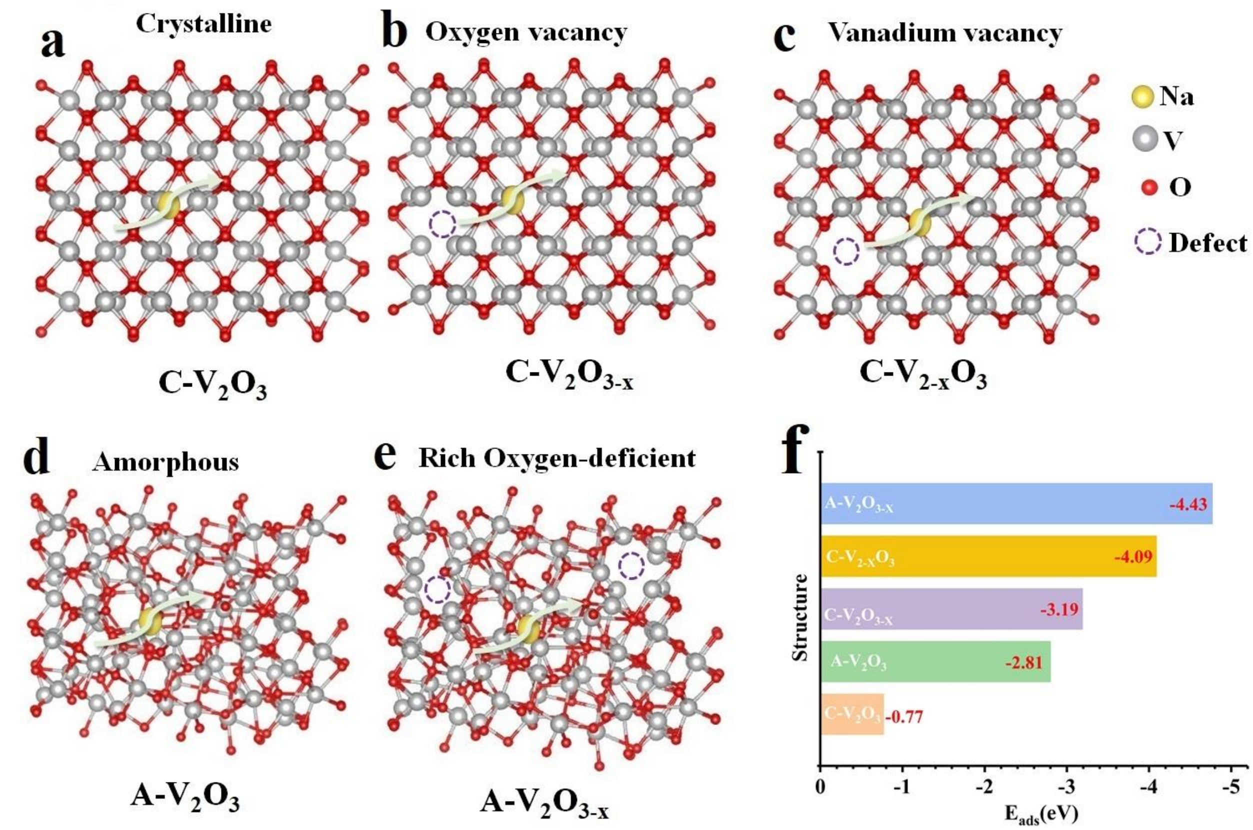


**Figure S17**. Structure models of Na diffusion in (a) C-$V_2O_3$ , (b) C-$V_2O_{3-x}$ , (c) C-$V_{2-x}O_3$ , (d) A-$V_2O_3$ ,(e) A-$V_2O_3$, and (f) their corresponding Na adsorption energies).

**Supplemental Table S1: Adsorption energy of Na in various $V_2O_3$ structures.**

| Structure | $E_{ads}$ (eV) |
|---|---|
| C-$V_2O_3$ | -0.77 |
| A-$V_2O_3$ | -2.81 |
| C-$V_2O_{3-x}$ | -3.19 |
| C-$V_{2-x}O_3$ | -4.09 |
| A-$V_2O_{3-x}$ | -4.43 |
| A/C-$V_2O_3$@C-HMCS | -1.77 |
| A/C-$V_2O_{3-x}$@C-HMCS | -4.77 |

## Theorectical discussion of Na in various $V_2O_3$ structures

The adsorption energy ($E_{ads}$) of the Na atom at amorphous structure is calculated to be -2.81 eV which is much lower than that of crystalline structure (-0.77 eV), indicating that porous isotropic amorphous phase is favorable for Na intercalation (Figure S17a,d). In addition, the Eads of C-$V_2O_{3-x}$ is even lower -3.19 eV (Figure S17b), which should be ascribed to oxygen vacancies, suggesting that the O-defective is highly beneficial for Na insertion. Distinctly,vanadium-deficient crystalline structure C-$V_{2-x}O_3$ displays lower Eads -4.09 eV than crystalline, amorphous, and O-deficient crystalline structure, resulting in higher adsorbing ability and faster kinetics of Na storage (Figure S17c). This enhancement is attributed to a higher coordination number and radius of the vanadium atom compared to the oxygen atom, which leads to enlarged $Na^+$ diffusion channels in the crystalline phase, thereby optimizing its kinetics. Further by combining the porous amorphous structure and oxygen-deficient, the A-$V_2O_{3-x}$ possesses a much lower $Na^+$ adsorption energy of -4.43 eV compared to all single structures counterparts (Figure S17e), suggesting A-$V_2O_{3-x}$ is the most energetically favorable for Na insertion. This result suggests that tailoring unsaturated coordination sites is an effective strategy to enhance the adsorption of $Na^+$ (Figure S17f, Table S1).

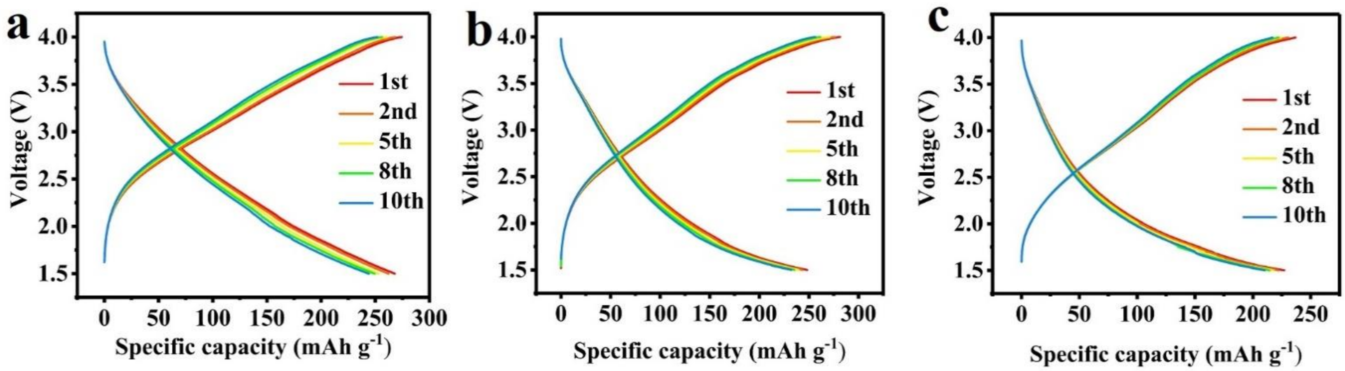


**Figure S18.** Discharge/charge profiles of (a) A/C-$V_2O_3$@C-HCS, (b) A/C-$V_2O_3$@C-WCS, and (c) A/C-$V_2O_3$@C-CS electrodes at 0.1 A $g^{-1}$.

**Supplemental Table 2:** Comparison of the electrochemical performance with reported A/C-V2O3@C-M based electrodes.

| **Cathode description** | **Capacity Retention (%, cycles No)** | **Rate performance (mAh $g^{-1}$)/ (A $g^{-1}$)** | **Average voltage (V)** | **Ref** |
|---|---|---|---|---|
| A/C-$V_2O_3$@C-CS core-shell | 93%,6000 | 92/10 | 2.6 | This work |
| A/C-$V_2O_3$@C-WCS core-shell | 100%,6000 | 123/10 | 2.7 | |
| A/C-$V_2O_3$@C-HCS core-shell | 100%,6000 | 155/10 | 2.8 | |
| A/C-$V_2O_{3-X}$@C-HMCS core-shell | 100%,6000 | 192/10 | 2.8 | |
| $NaV_6O_{15}$ /MWCNTs nanotube | 96%,500 | 123.7/10 | 2.7 | [1] |
| A-$V_2O_5$/C-WCS core-shell | 95%,3000 | 148/5.0 | 3.0 | [2] |
| Bilayered $V_2O_5$ | 85%,320 | 150/0.63 | 3.0 | [3] |
| Additive-free $V_2O_5$ thin film | 100%,200 | 124/5.0 | -0.25 | [4] |
| $Co_{0.16}Zn_{0.09}V_2O_5 \cdot nH_2O$ | 97%,1000 | 90/3.0 | 0.7 | [5] |
| cG/VO microspheres | 73%,2000 | 214/4.0 | 1.0 | [6] |
| $VS_4$ Nanoparticles | 84%,1200 | 188.1/4.0 | 1.2 | [7] |
| $NaV_6O_{15}$ nanotube | 94%,3000 | 105/2.5 | 2.5 | [8] |
| $NaVOPO_4$ layered | 67%, 1000 | 57/0.73 | 3.3 | [9] |
| $Na_{0.282}V_2O_5$ nanorods | 99%,1000 | 80/0.3 | 2.7 | [10] |
| $Na_{1.25}V_3O_8$ nanowires | 87%,1000 | 76/2.0 | 2.4 | [11] |
| $Na_3V_2(PO_4)_3$ spheres | 87.5%,1000 | 96/2.0 | 3.35 | [12] |
| $Na_3V_2(PO_4)_2O_2F$ nanotetraprisms | 81%,2000 | 84/5.2 | 3.8 | [13] |
| $Na_3V_2(PO_4)_2O_2F$ carbon cloth | 95%,1500 | 84/1.2 | 3.8 | [14] |
| $Na_3V_2(PO_4)_2F_3$ microcubes | 98%,2000 | 53/2.2 | 3.6 | [15] |
| $Na_6Fe_5(SO_4)_8$/CNTs nano-architectured | 100.8%,1000 | 86.4/ 0.24 | 3.6 | [16] |

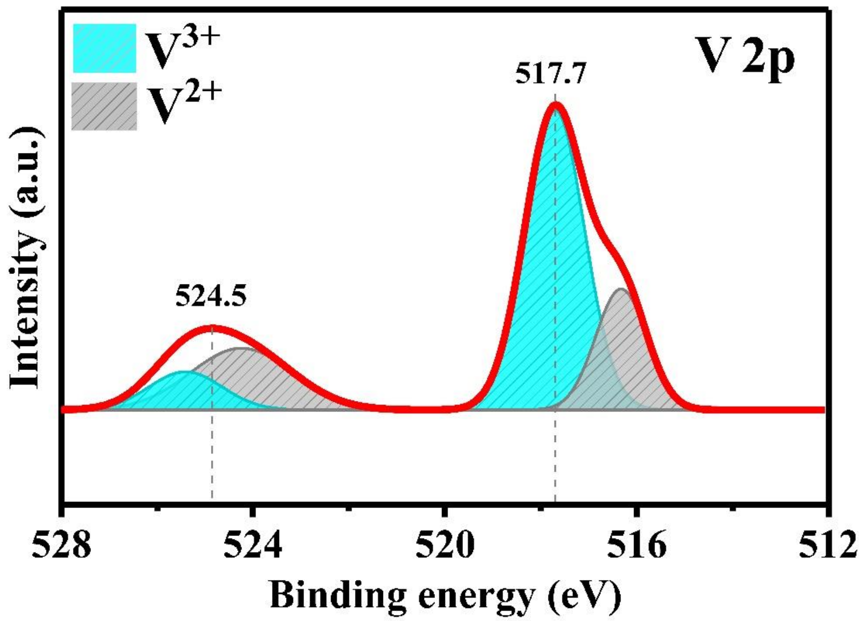


**Figure S19.** XPS spectrum of V 2p with 100 cycles for A/C-$V_2O_{3-x}$@C-HMCS electrode.

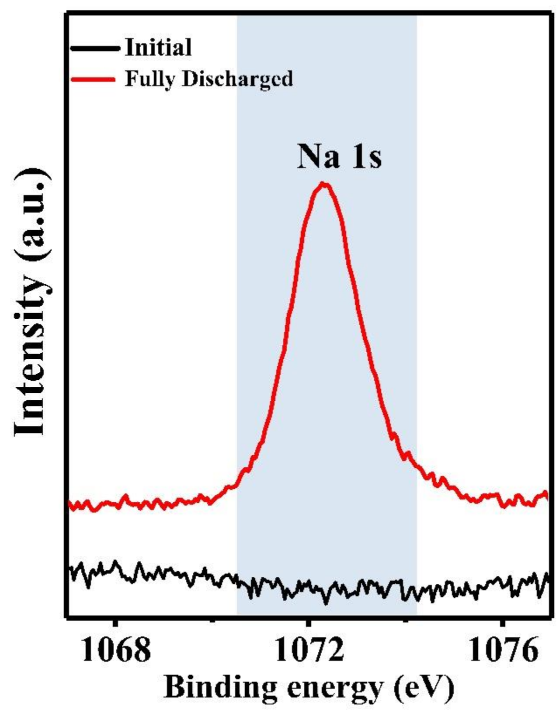


**Figure S20.** Ex-situ XPS Na 1st spectra of A/C-$V_2O_{3-x}$@C-HMCS electrodes at full discharge–stage (1.5 V).

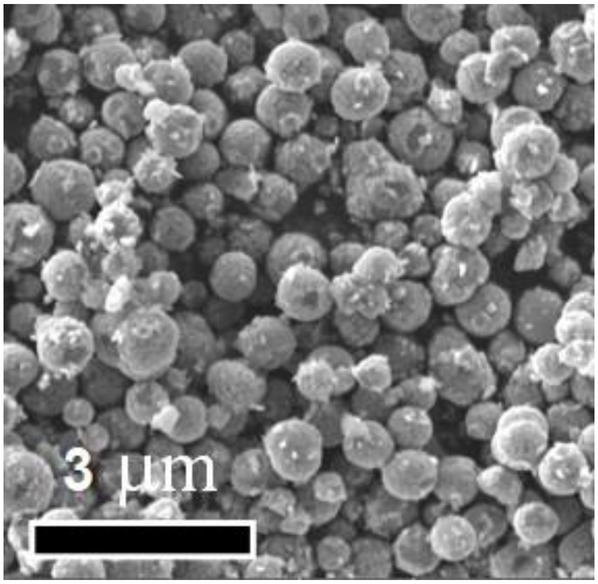


**Figure S21.** SEM images of A/C-$V_2O_{3-x}$@C-HMCS after 1000 cycles.

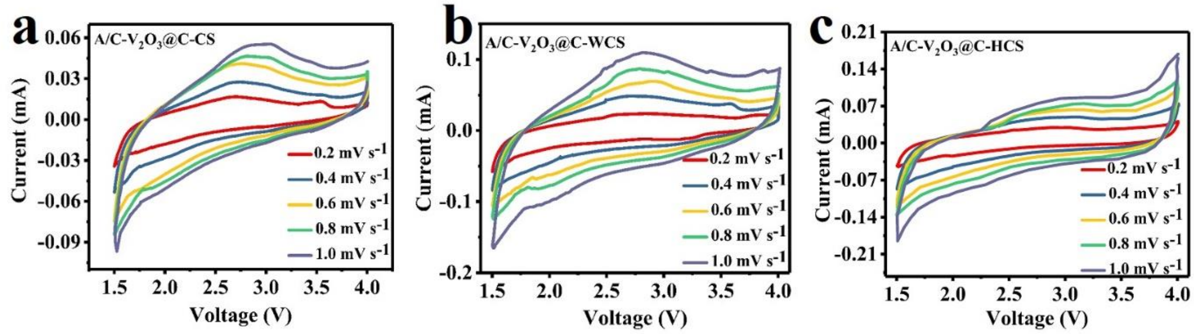


**Figure S22.** CV profiles at different scan rates (0.2-1.0 mV $s^{-1}$) between 1.5-4.0 V (versus $Na^+$/Na) of A/C-$V_2O_3$@C-CS, A/C-$V_2O_3$@C-WCS, and A/C-$V_2O_3$@C-HCS cathodes.

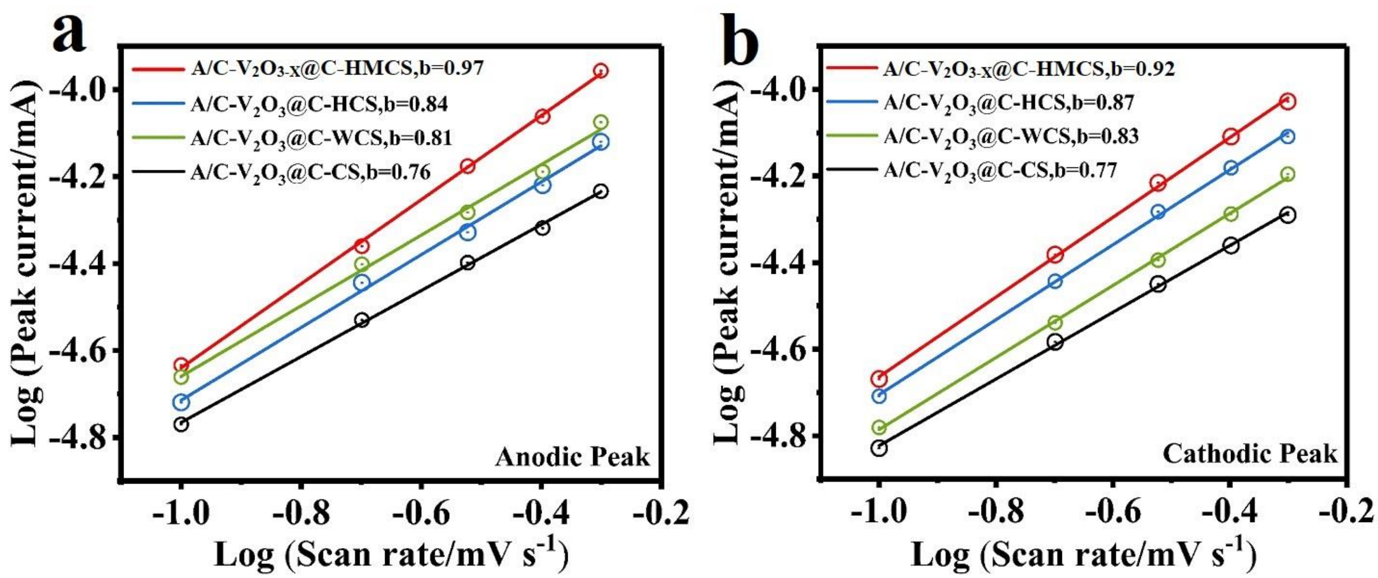


**Figure S23.** Calculated b-values from log (peak current) versus log (scan rate) plots for A/C-$V_2O_3$@C-CS, A/C-$V_2O_3$@C-WCS, A/C-$V_2O_3$@C-HCS, and A/C-$V_2O_{3-x}$@C-HMCS.

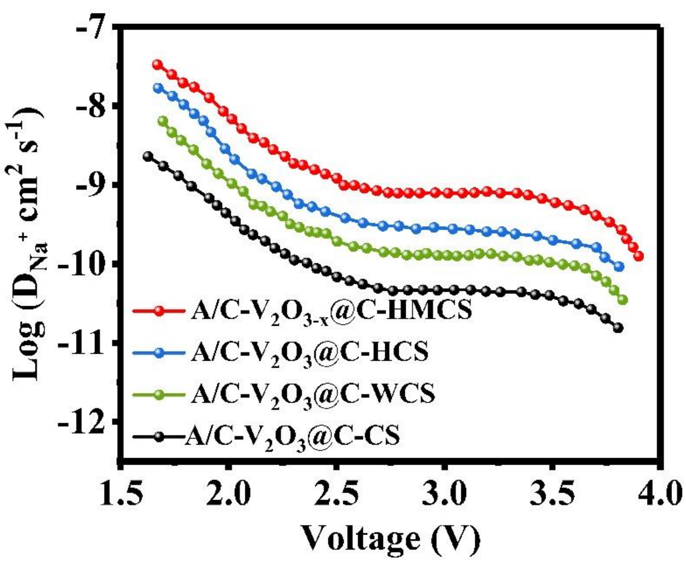


**Figure S24.** Diffusion coefficients calculated from the GITT during the desodiation process of A/C-$V_2O_3$@C-CS, A/C-$V_2O_3$@C-WCS, A/C-$V_2O_3$@C-HCS, and A/C-$V_2O_{3-x}$@C-HMCS.

**REFERENCES***


[1] S. Osman, S. Zuo, X. Xu, J. Shen, Z. Liu, F. Li, P. Li, X. Wang, J. Liu, *ACS Appl. Mater. Interfaces* **2021**, 13, 816.

[2] S. Osman, C. Peng, J. Shen, F. Li, W. Huang, J. Liu, J. Liu, D. Xue, M. Zhu, *Nano Energy* **2022**, 107481.

[3] S. Tepavcevic, H. Xiong, V. R. Stamenkovic, X. Zuo, M. Balasubramanian, V. B. Prakapenka, C. S. Johnson, T. Rajh, *ACS Nano* **2012**, 6, 530.

[4] Y. Li, C. Liu, Z. Xie, J. Yao, G. Cao, *J. Mater. Chem. A.* **2017**, 5, 16590.

[5] H. Huang, T. Tian, L. Pan, X. Chen, E. Tervoort, C.-J. Shih, M. Niederberger, *J. Mater. Chem. A.***2019**, 7, 16109.

[6] B. Yan, X. Li, Z. Bai, L. Lin, G. Chen, X. Song, D. Xiong, D. Li, X. Sun, *J. Mater. Chem. A.* **2017**, 5, 4850.

[7] Q. Pang, Y. Zhao, Y. Yu, X. Bian, X. Wang, Y. Wei, Y. Gao, G. Chen, *ChemSusChem* **2018**, 11, 735.

[8] X. Song, J. Li, Z. Li, Q. Xiao, G. Lei, Z. Hu, Y. Ding, H. M. Kheimeh Sari, X. Li, *ACS Appl. Mater. Interfaces* **2019**, 11, 10631.

[9] Y. Fang, Q. Liu, L. Xiao, Y. Rong, Y. Liu, Z. Chen, X. Ai, Y. Cao, H. Yang, J. Xie, C. Sun, X. Zhang, B. Aoun, X. Xing, X. Xiao, Y. Ren, *Chem* **2018**, 4, 1167.

[10] Y. Cai, J. Zhou, G. Fang, G. Cai, A. Pan, S. Liang, *J. Power Sources* **2016**, 328, 241.

[11] Y. Dong, S. Li, K. Zhao, C. Han, W. Chen, B. Wang, L. Wang, B. Xu, Q. Wei, L. Zhang, X. Xu, L. Mai, *Energy Environ. Sci.* **2015**, 8, 1267.

[12] R. Gao, R. Tan, L. Han, Y. Zhao, Z. Wang, L. Yang, F. Pan, *J. Mater. Chem. A.* **2017**, 5, 5273.

[13] J.-Z. Guo, P.-F. Wang, X.-L. Wu, X.-H. Zhang, Q. Yan, H. Chen, J.-P. Zhang, Y.-G. Guo, *Adv. Mater.* **2017**, 29, 1701968.

[14] J.-Z. Guo, A.-B. Yang, Z.-Y. Gu, X.-L. Wu, W.-L. Pang, Q.-L. Ning, W.-H. Li, J.-P. Zhang, Z.-M. Su, *ACS Appl. Mater. Interfaces* **2018**, 10, 17903.

[15] Y. Cai, X. Cao, Z. Luo, G. Fang, F. Liu, J. Zhou, A. Pan, S. Liang, *Adv Sci (Weinh)* **2018**, 5, 1800680.

[16] S. Li, X. Song, X. Kuai, W. Zhu, K. Tian, X. Li, M. Chen, S. Chou, J. Zhao, L. Gao, *J. Mater. Chem. A.* **2019**, 7, 14656.